Available online at www.sciencedirect.com
ScienceDirect
Trans. Nonferrous Met. Soc. China 34(2024) 3221−3232
Transactions of Nonferrous Metals Society of China
www.tnmsc.cn

# Microstructure and mechanical properties of continuous drive friction welded $Ti_2AlNb$ alloy under different rotational rates

Zhi-qiang BU[1], Xiu-ping MA[2], Jia-yun WU[2], Zhen LÜ[2], Hu CHEN[1], Jin-fu LI[1]

1. State Key Laboratory of Metal Matrix Composites, School of Materials Science and Engineering, Shanghai Jiao Tong University, Shanghai 200240, China;
2. AECC South Industry Company Limited, Zhuzhou 412002, China

Received 7 April 2023; accepted 20 September 2023

**Abstract:** $Ti_2AlNb$-based alloy was joined in a continuous drive friction welding machine under different rotational rates (500, 1000 and 1500 r/min). The microstructure and mechanical properties of the joints were investigated. It is shown that the weld zone (WZ) is fully composed of recrystallized *B*2 phase, and the grain size decreases with increasing rotational rate. The thermo-mechanically affected zone (TMAZ) suffers severe deformation during welding, due to which most of original precipitation phase is dissolved and streamlines are present. In the heat affected zone (HAZ), only the fine *O* phase is dissolved. The as-welded joint produced using 1000 r/min has the best mechanical properties, whose strength and elongation are both close to those of the base metal, while the as-welded joint obtained using 500 r/min exhibits the worst mechanical properties. Post-weld annealing treatment annihilates the deformation microstructure and fine *O* phase precipitates in the joints, consequently improving the mechanical properties significantly. Decomposed $\alpha_2$ phase is a weakness for the mechanical performance of the joint since microcracks are apt to form in it in the tensile test.

**Key words:** $Ti_2AlNb$ alloy; continuous drive friction welding; microstructure; mechanical properties

## 1 Introduction

$Ti_2AlNb$-based alloy as a latecomer in titanium−aluminum intermetallic alloys was first discovered in 1988 [1−3]. $Ti_2AlNb$-based alloy has better room-temperature ductility, processability and fracture toughness compared with TiAl alloy and higher elevated temperature oxidation and creep resistances than $Ti_3Al$ alloy [4−8]. Meanwhile, its density is about 40% lower than that of nickel-based superalloys [9,10]. All these excellent comprehensive performances endow this type of material with a great application prospect in the field of aerospace. $Ti_2AlNb$-based alloy has thus attracted much attention over the past three decades [11−15].

The practical application of $Ti_2AlNb$-based alloy is inseparable from welding processing. Heretofore the investigations were mainly been focused on the fusion welding [11,16−20]. An insurmountable drawback with fusion welding is that the loss of ductility is too severe in the fusion zone especially at elevated temperature due to lack of adequate means to control the microstructure. Continuous drive friction welding (CDFW) is a solid-state welding method, in which the joint metal is plasticized under the friction heat, and undergoes local deformation and dynamic recrystallization subsequently. The forged microstructure around the weld line is expected to be advantageous to the mechanical properties of the welded joint [21−24].

CDFW has been widely used to join metallic

**Corresponding author:** Jin-fu LI, Tel/Fax: +86-21-54748530, E-mail: jfli@sjtu.edu.cn
DOI: 10.1016/S1003-6326(24)66604-5

materials, such as steels, titanium alloys, nickel-based alloys, and aluminum alloys [21,25−28], while very few works of CDFW joined $Ti_2AlNb$-based alloy have been published so far. Even so ones can still obtain some enlightenment from the CDFW process of other alloys. ÖZDEMIR et al [21] investigated the effect of rotational rate on interface properties of friction-welded dissimilar steel joint, and the results showed that the width of fully plasticized deformed zone was mainly affected by the rotational rate. A higher rotational rate and shorter friction time always increased the tensile strength of welded joints. SATHIYA et al [22] studied the mechanical and metallurgical properties of friction welded AISI 304 stainless steel. As the friction time increased, the width of the recrystallization zone increased, but the strength of joint decreased. ATES et al [23] friction welded MA956 superalloy. The tensile strength of joints was found to increase up to a certain value with increasing friction pressure and the best mechanical properties were obtained with the friction pressure higher than 50 MPa. LIANG et al [27] investigated the CDFW of 5A33 Al to AZ31B Mg alloy and found that the thickness of reaction layer first increased and then decreased with increasing friction time. LI and WANG [28] simulated the CDFW of 20 mild steel by a 2D finite element model. The results indicated that the rotational rate and axial pressure had a great influence on the interface temperature and axial shortening. It is clear that the quality of friction welded joints is closely related with the processing parameters including rotational rate, friction pressure, upsetting pressure, friction time, and so on, and it is crucial to understand how these factors affect the mechanical properties of the welded joints.

In this study, CDFW was applied to joining the $Ti_2AlNb$-based alloy and the effect of rotational rate on the microstructure and tensile mechanical properties of the welded joints was especially concerned. The potential of post-weld heat treatment (PWHT) in improving the mechanical performance of the welded joints was also explored.

## 2 Experimental

The nominal composition of the base metal used for welding is Ti−22Al−23Nb−1Mo−1Zr (at.%). Table 1 gives the chemical composition of the experimental alloy, indicating that the error in composition is acceptable. The alloy was machined to cylinders with a dimension of $d$25 mm × 85 mm for the CDFW experiment. The schematic diagram of CDFW process is shown in Fig. 1(a), and the friction welder (C320) used in the present

**Table 1** Chemical composition of $Ti_2AlNb$ based alloy (at.%)

| Al | Nb | Zr | Mo | Ti |
|---|---|---|---|---|
| 21.58 | 23.17 | 1.08 | 0.98 | Bal. |

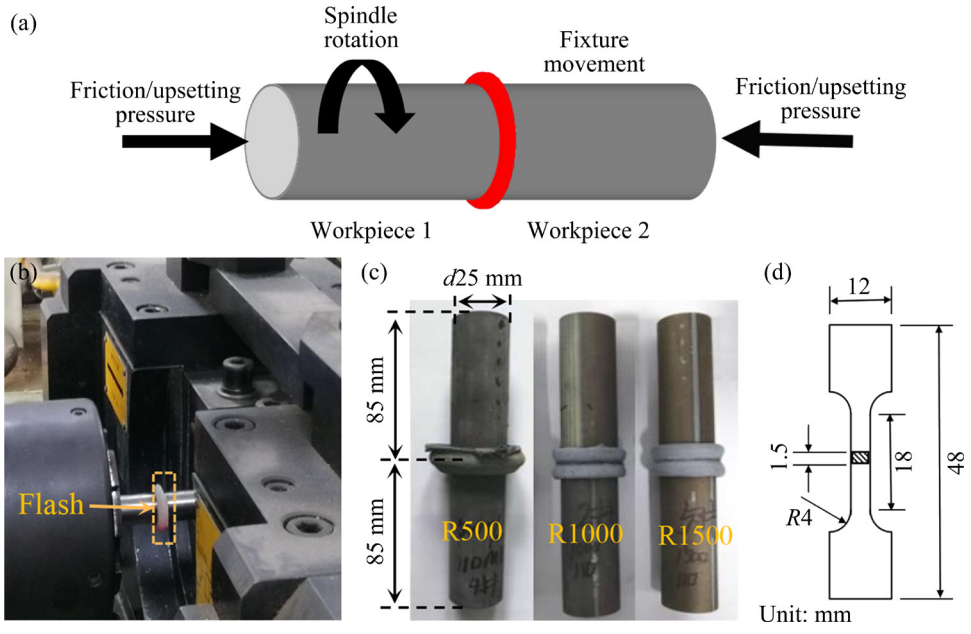


**Fig. 1** Schematic diagram of CDFW (a), photo of friction welder (b), photos of joints under different rotational rates (c) and geometry of tensile specimen (d)

experiment is shown in Fig. 1(b). The welding surfaces were polished and cleaned in an ethanol solution. In CDFW, Workpiece 1 installed on the spindle rotated at a constant rate, while Workpiece 2 installed on the fixture moved in the axial direction with an axial force applied. The frictional heat plasticized the interfacial material, and part of the plasticized material was extruded from the weld interface under the friction pressure forming the weld flash. The rotation was stopped as soon as the predetermined distance of movement was reached, and an upsetting pressure was applied immediately to achieve welding.

Table 2 presents the welding parameters. The friction pressure was 100 MPa, the axial shortening was 5 mm, and the upsetting pressure was 180 MPa. Three different rotational rates, 500, 1000 and 1500 r/min, were investigated in the experiment. For the sake of simplicity, R500, R1000 and R1500 were used to represent the corresponding samples (joints) in the following. Figure 1(c) shows the joints welded with different rotational rates. It can be seen that the flash of R1000 and R1500 joints is symmetrical while the flash of R500 joints is irregular. After welding, part of the joints were annealed at 810 °C for 2 h followed by air cooling. The specimens for microstructure investigation were prepared by electrochemically polishing with a solution of 6% perchloric acid, 34% butarol and 60% carbinol. The microstructure was observed in a scanning electron microscope (SEM) equipped with electron backscattered diffraction (EBSD) detector. EBSD measurements were conducted with a step size of 0.3−0.5 μm. Tensile test was performed in a universal material testing machine with a strain rate of $1.0\times10^{-3}\ s^{-1}$ and the geometry of the tensile specimen is depicted in Fig. 1(d).

**Table 2** Processing parameters of CDFW

| Sample | Rotational rate/ ($r\cdot min^{-1}$) | Friction pressure/ MPa | Axial shortening/ mm | Upsetting pressure/ MPa |
|---|---|---|---|---|
| R500 | 500 | 100 | 5 | 180 |
| R1000 | 1000 | 100 | 5 | 180 |
| R1500 | 1500 | 100 | 5 | 180 |

## 3 Results and discussion

### 3.1 Microstructure of as-welded joints

The microstructure of the base metal is composed of irregular granular $\alpha_2$, besides thick lamellar *O* phase and fine acicular *O* phase embedded in the matrix *B*2 phase, as shown in Fig. 2.

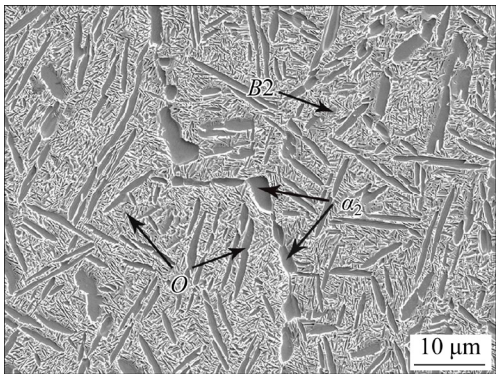


**Fig. 2** Microstructure of base metal

The SEM images of the joints welded under different rotational rates are presented in Fig. 3. A joint can be divided into different zones: weld zone (WZ), thermo-mechanically affected zone (TMAZ) and heat affected zone (HAZ), based on the microstructure characteristics. The phase constitution and morphology vary greatly from one zone to another, due to the different thermal history during the welding.

The WZ, located in the middle of the joint, as shown in Figs. 3($a_1$−$c_1$), is merely composed of the recrystallization grains of *B*2 phase. The disappearance of a phase from the joint implies that it is locally reheated above the phase transformation temperature. From the microstructure of as-weld joints, it is known that the friction heat elevates the temperature of WZ above the *B*2 transformation temperature [29], so both *O* and $\alpha_2$ phases transform into *B*2 phase during the welding. Our previous study [30] has shown that the critical cooling rate to retain the elevated temperature *B*2 phase is 4 °C/s. It has also been reported that the highest cooling rate can reach 350−400 °C/s when friction-welding titanium alloys [31], which is much higher than the critical cooling rate for *O* phase to precipitate. Therefore, only single *B*2 phase can be detected in WZ. Under a given friction pressure, a faster rotational rate can generate more friction heat within a unit of time, and the time to reach the maximum temperature is decreased [26,28], due to which the interfacial material can be heated faster to the plastic temperature. The axial shortening is controlled in the present study. Thus, a higher

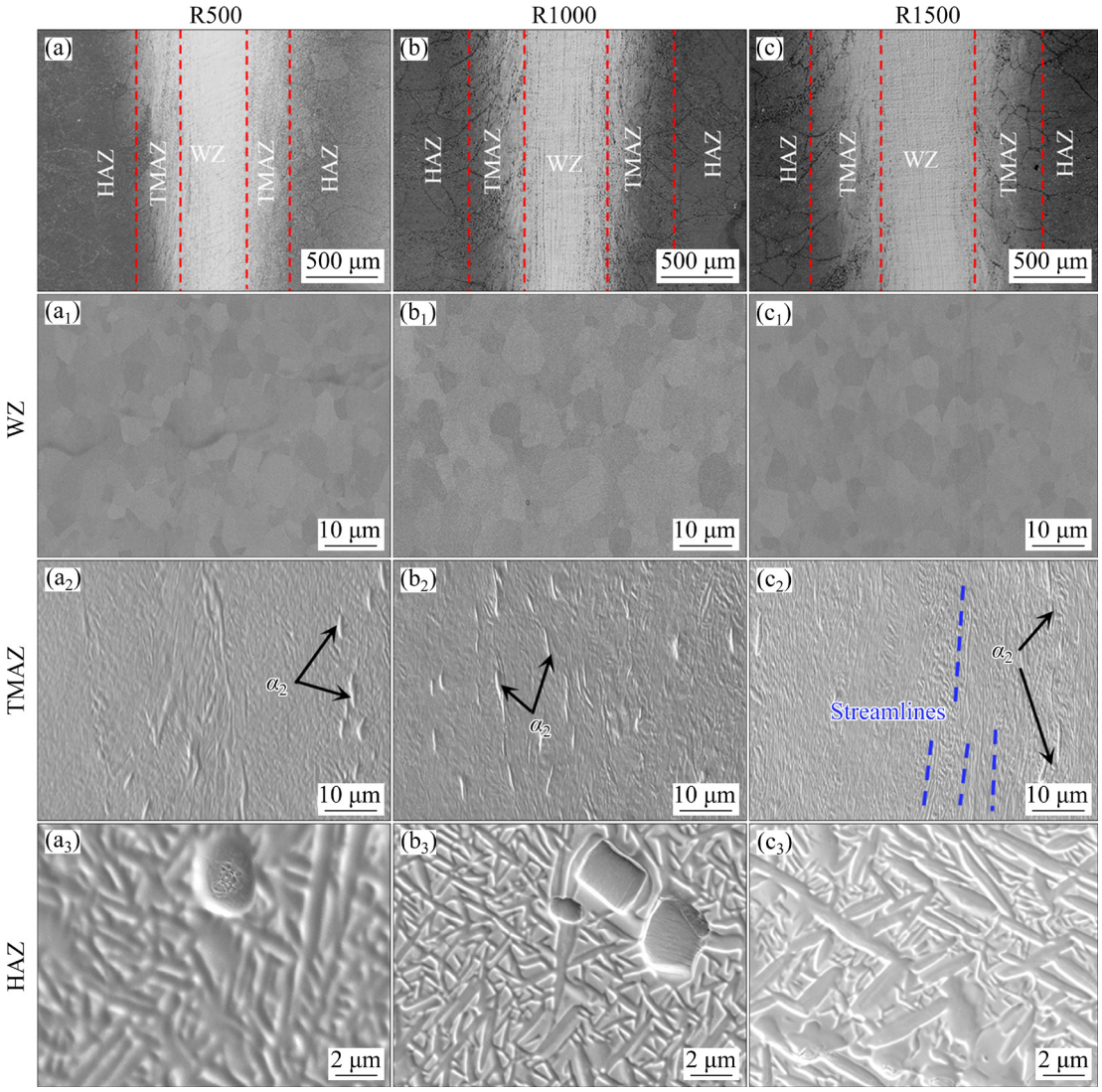


**Fig. 3** Microstructures of as-welded joints under different rotational rates: (a, $a_1$−$a_3$) 500 r/min; (b, $b_1$−$b_3$) 1000 r/min; (c, $c_1$−$c_3$) 1500 r/min

rotational rate means a shorter welding time. The shorter retention time at high temperature makes the grain size decrease with increasing rotational rate. R500 experiences the longest welding time in this study, and the *B*2 grains in WZ are the largest.

The TMAZ is on both sides of the WZ. The material within TMAZ is heated into *B*2+$\alpha_2$ phase region or higher [32], and deforms under the shear and axial force. Consequently, most of original *O* phase transforms into *B*2 phase, along with the elongated $\alpha_2$ phase and residual *O* phase (Figs. 3($a_2$−$c_2$)). The shear force increases with increasing rotational rate so that the TMAZ of R1500 contains the most streamlines (Fig. 3($c_2$)). However, more precipitates survive in the TMAZ of R1500 due to the shortest welding time.

The HAZ is such an area within which the temperature is elevated enough to influence the microstructure but no obvious plastic deformation takes place. Thus, only some precipitates are decomposed during the welding. The resultant HAZ consists of residual granular $\alpha_2$ phase, relatively thick *O* phase and *B*2 base phase, as shown in Figs. 3($a_3$−$c_3$). At a slower rotational rate, more precipitates are dissolved. It can be seen that the original fine acicular *O* phase is dissolved on a large scale and the coursed lamellar *O* phase becomes larger in R500. In contrast, some residual fine *O* phase can be seen in R1500 (Fig. 3($c_3$)). Decomposed $\alpha_2$ phase is detected in R500, as shown in Fig. 3($a_3$), meaning that $\alpha_2$ phase is unstable in HAZ if the welding time is longer.

WANG et al [33] reported that the granular $\alpha_2$ phase could decompose into $\alpha_2$+*O* phase during the isothermal heat treatment of $Ti_2AlNb$ alloy. The decomposition of $\alpha_2$ phase during welding worsens the mechanical properties.

The microstructure of WZ was analyzed in detail using EBSD and the results are shown in Fig. 4. *B*2 grains are randomly oriented and they are refined obviously compared to the base metal (Figs. 4(a−c)), indicating the occurrence of recrystallization during the welding. The *B*2 grains are in principle equiaxed. The average grain size under each rotational rate is shown in Fig. 4(d). It decreases gradually from 5.2 μm in R500 to 4.5 μm in R1000 and to 3.7 μm in R1500. The disorientation angle distribution of grains in WZ was further analyzed. By taking 15° as the critical disorientation angle, grain boundaries can be classified into high-angle grain boundaries (HAGBs) and low-angle grain boundaries (LAGBs). The fraction of HAGBs decreases from 83.1% in R500 to 74.1% in R1500. R500 experiences a longer welding time, which permits higher-level recrystallization in the WZ [34]. As a result, the *B*2 grains in the WZ of R500 have the largest size and disorientation angle.

Figure 5 shows the EBSD analysis results of the microstructure near the boundary of WZ and TMAZ in R1500. The microstructure is extremely uneven in TMAZ. The severe plastic deformation

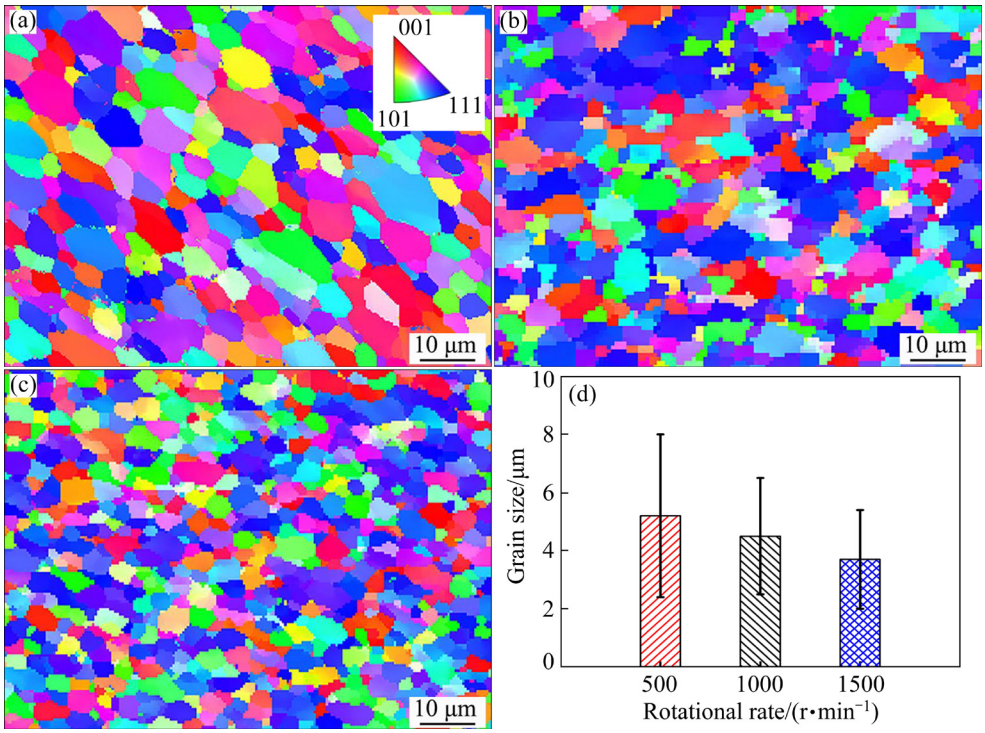


**Fig. 4** Inverse pole figure (IPF) of WZ in R500 (a), R1000 (b) and R1500 (c), and average grain size of *B*2 phase (d)

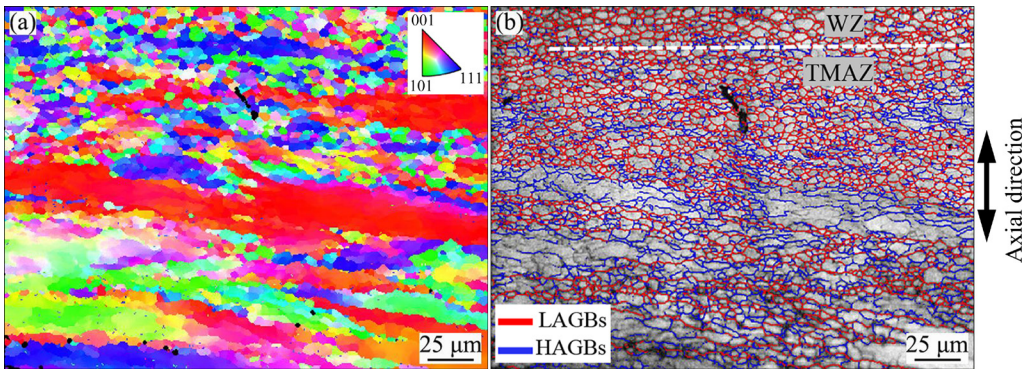


**Fig. 5** EBSD mapping of microstructure near boundary of WZ and TMAZ in R1500: (a) Inverse pole figure; (b) Grain boundary distribution map

elongates the grains and propels them to distribute along the direction perpendicular to the axial direction (Fig. 5(a)). The existence of refined recrystallization grains and deformation streamlines in TMAZ indicates that partial recrystallization occurs in the microstructure, driven by the accumulated dislocations. As the deformation degree and temperature rise in TMAZ are lower than those in WZ, full dynamic recrystallization cannot take place in TMAZ. Because of the nonuniform deformation in TMAZ, recrystallization merely occurs in the severely deformed area and fine equiaxed *B*2 grains are formed. Numerous LAGBs to be presented in TMAZ (Fig. 5(b)) mean lots of substructure. This plays an important role in the tensile property of the joint, especially for R1500 with the largest deformation degree (Fig. 3($c_2$)).

### 3.2 Mechanical properties of as-welded joints

The tensile stress−strain curves of the base metal and the joints welded under various rotational rates are presented in Fig. 6. It can be seen that the mechanical property of the joints is highly dependent on the welding parameters. Both tensile strength and elongation increase firstly and then decrease with increasing rotational rate. R500 has the poorest mechanical property, i.e., the tensile strength and elongation only reach 63% and 15% of the base metal, respectively. R1000 behaves the best. The tensile strength and elongation are close to those of the base metal. For R1500, both yield and ultimate strengths are compared to those of R1000. However, the elongation is decreased dramatically.

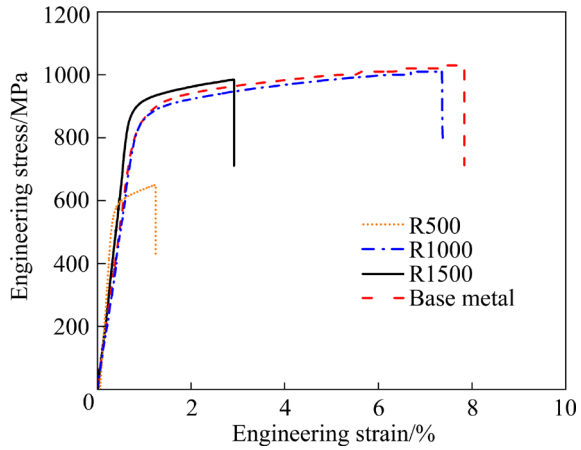


**Fig. 6** Tensile engineering stress−strain curves of as-welded joints, with base metal for comparison

The fractured samples are shown in Fig. 7. It can be seen that fracture takes place in HAZ for R500. Cracks propagate along the grain boundary during the test (Fig. 7(b)). As marked by blue circles in Fig. 7(b), decomposed $\alpha_2$ phase exists near the fracture, and some of the grains are with cracks. It is very possible that the fracture starts from the decomposed $\alpha_2$ phase, and the presence of decomposed $\alpha_2$ phase greatly influences the mechanical performance. When R1000 is subjected to the test, fracture occurs far away from the weld interface. Form the microstructure shown in Fig. 7(d), it is known that the sample fractures in the base metal. In contrast, the fracture surface is flat in R1500. As shown in Fig. 7(e), the sample fractures in TMAZ, and cracks propagate along the streamlines.

Figure 8 shows the fracture morphologies of the joints. Many intergranular cracks present and fewer dimples and tearing ridges can be observed on the fracture of R500 (Figs. 8(a, d)). It is clear that R500 fractures through a mixed mode of cleavage and intergranular fractures, and the intergranular fracture plays a dominant role [35]. Because the fine original precipitation phase is dissolved seriously in HAZ, as shown in Fig. 3($a_3$), cracks propagates along the grain boundary of the course HAZ microstructure (Fig. 8(b)). Eventually, the joint is broken prematurely and exhibits the worst tensile property.

The fracture surface is changed a lot for R1000. There are many river patterns, cleavage planes and fine dimples on the fracture (Figs. 8(b, e)). The joint fractures in a quasi-cleavage fracture mode, exhibiting the best elongation in the test. In R1500, large planes and fewer tearing ridges can be seen on the fracture (Figs. 8(c, f)). Brittle fracture takes place in the test. Streamlines generated during CDFW result in the heaviest anisotropy in the TMAZ microstructure of R1500, which greatly worsens the mechanical property in the axial direction of the sample [36]. The inhomogeneous structure in TMAZ, as shown in Fig. 5, inevitably causes stress concentration, which is unfavorable for the mechanical property.

### 3.3 Effect of annealing

Typical microstructures of as-annealed joints are shown in Fig. 9. The grain size of *B*2 phase in WZ, TMAZ and HAZ is basically unchanged due to

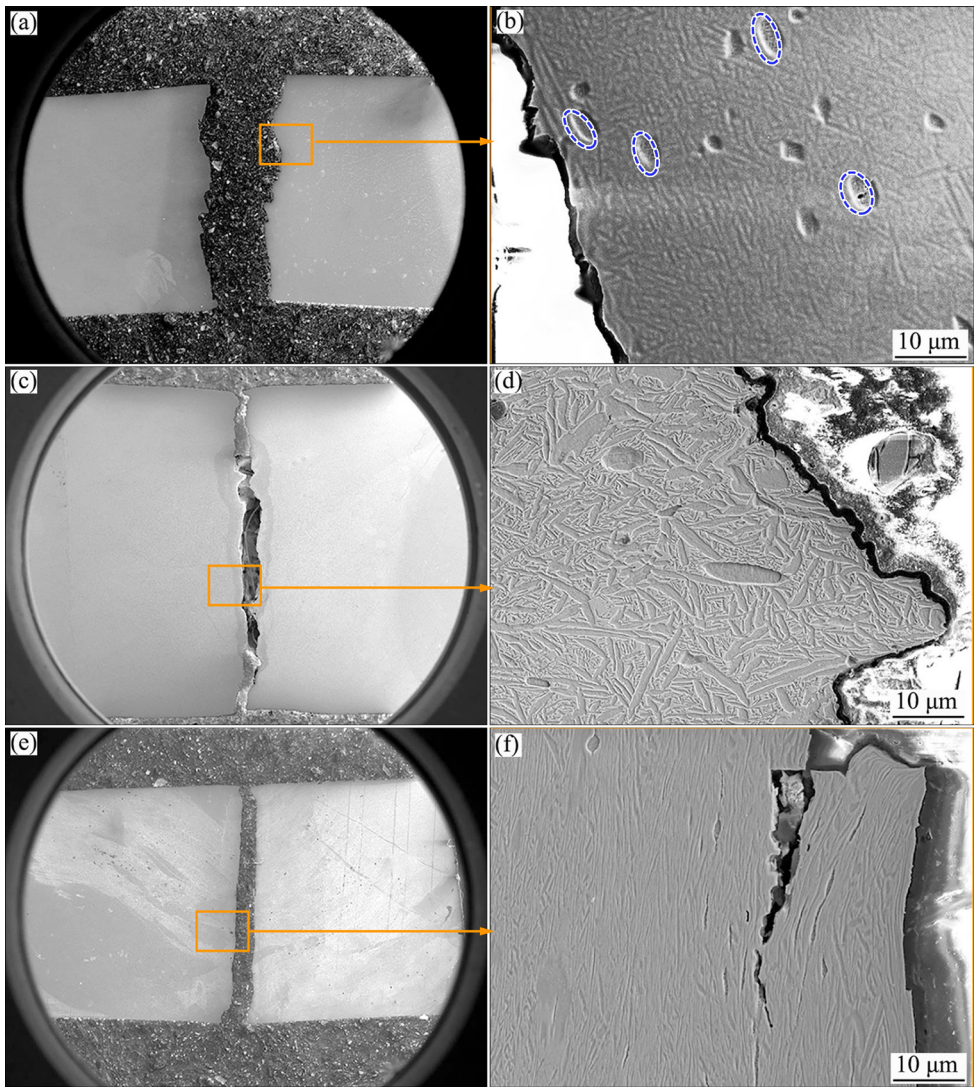


**Fig. 7** SEM images of fractured as-welded joints: (a, b) R500; (c, d) R1000; (e, f) R1500

the annealing treatment, but the annealing greatly influences the precipitation phases. The *O* phase precipitated in the WZ of R500 is slightly thicker than in R1500. The deformation microstructures such as streamlines disappear from TMAZ and instead a large amount of tiny *O* phase is precipitated. In HAZ, lots of fine acicular *O* plates are precipitated around the large residual *O* phase. The $\alpha_2$ phase in TMAZ and HAZ is basically unchanged due to annealing (Figs. 9($a_2$–$c_2$, $a_3$–$c_3$)). The *O* phase in the base metal to form the weld joint is completely or partially dissolved during the welding (Fig. 3). Limited by the short welding time, solute diffusion is inadequate and a severe concentration fluctuation exists in the welded joint, which provides plenty of nucleation sites for the re-precipitation of *O* phase during the annealing process. Therefore, a high density of *O* phase is re-precipitated in the joint.

The average tensile strength and elongation of as-welded and as-annealed joints with different welding parameters are shown in Fig. 10. The annealing treatment improves the mechanical property of the welded joints effectively, especially for R500 and R1500. The tensile strength and elongation of R500 increase from 652 MPa and 2.6% to 975 MPa and 6.07%, respectively. The elongation of R1500 increases from 2.9% to 7.58%. The elongation increments in R500 and R1500 are both larger than 100%. In comparison, the tensile strength and elongation of R1000 merely increase form 1010 MPa and 7.4% to 1023 MPa and 7.86%, respectively. Even so, R1000 still possesses the best comprehensive mechanical property after the heat treatment.

Figure 11(a) shows the photographs of as-

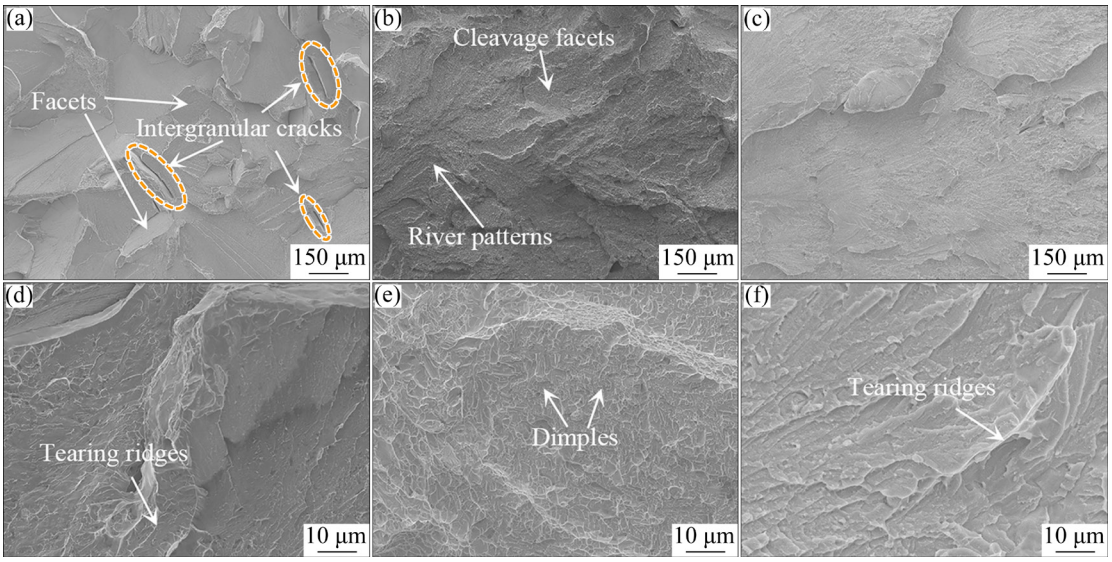


**Fig. 8** SEM images of fracture in as-welded joints: (a, d) R500; (b, e) R1000; (c, f) R1500

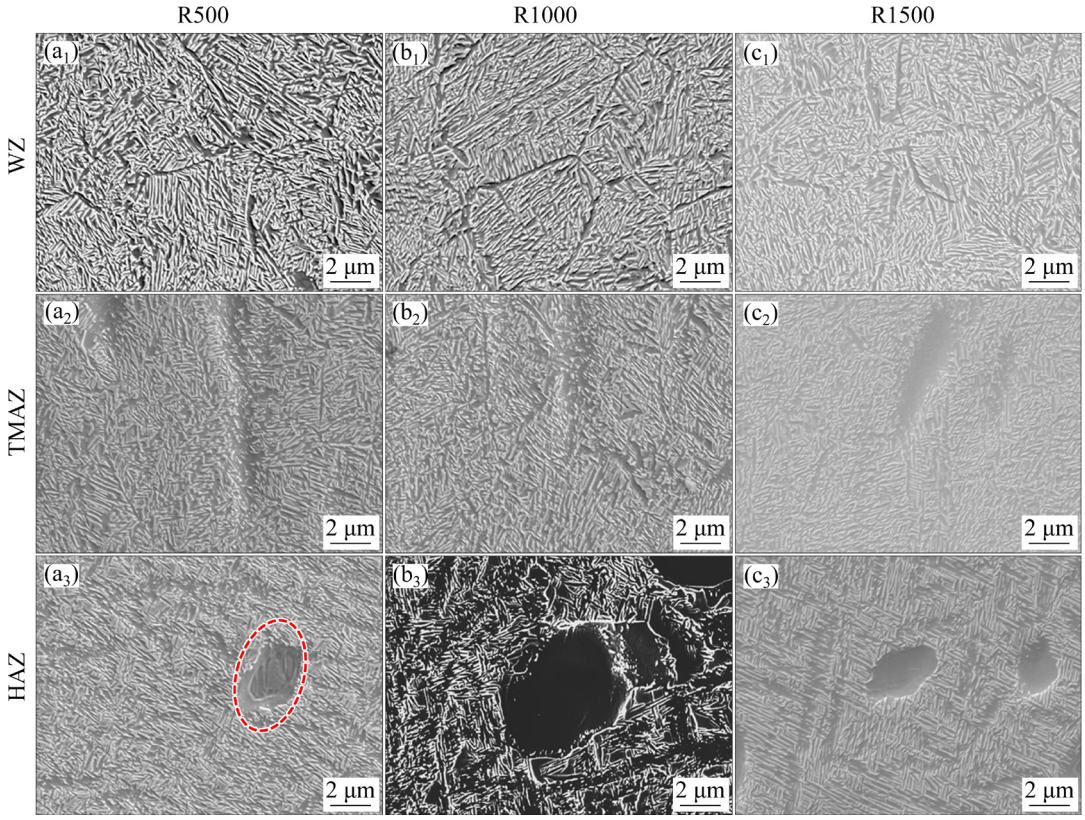


**Fig. 9** Microstructures of as-annealed joints

annealed joints after the tensile test. It can be seen that deformation mainly occurs in the base metal rather than in the welding area (WZ+TMAZ+ HAZ) during the tensile test. Specially, R500 fractures in the HAZ, as shown in Figs. 11(b−d), while R1000 and R1500 fracture in the base metal. At large magnification, many cracks can be observed in the area near the fracture surface of R500. As a rule, the cracks are preferentially generated in the decomposed $\alpha_2$ phase, as indicated by the inserted image of Fig. 11(d). The microstructure originated from the decomposition of $\alpha_2$ phase is undoubtedly the weak area in the tensile test. The fracture of as-annealed R500 is shown in Fig. 12. Different

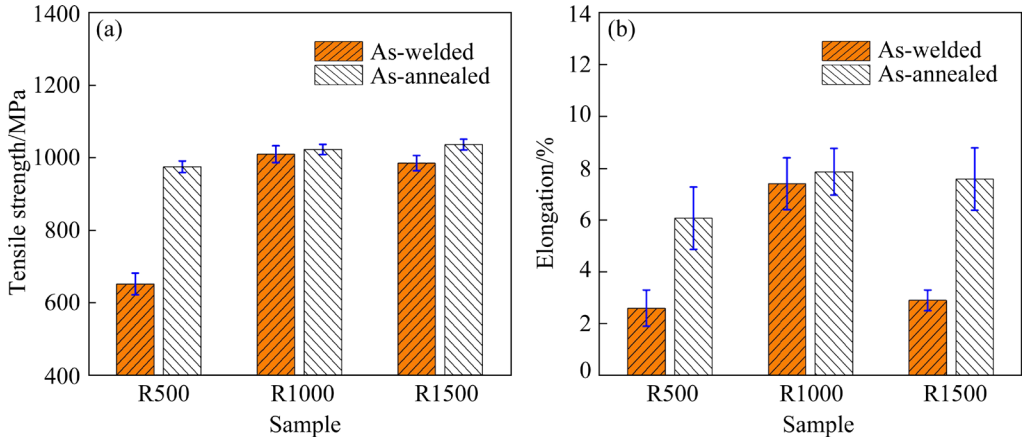


**Fig. 10** Comparison of mechanical properties of as-welded and as-annealed joints: (a) Tensile strength; (b) Elongation

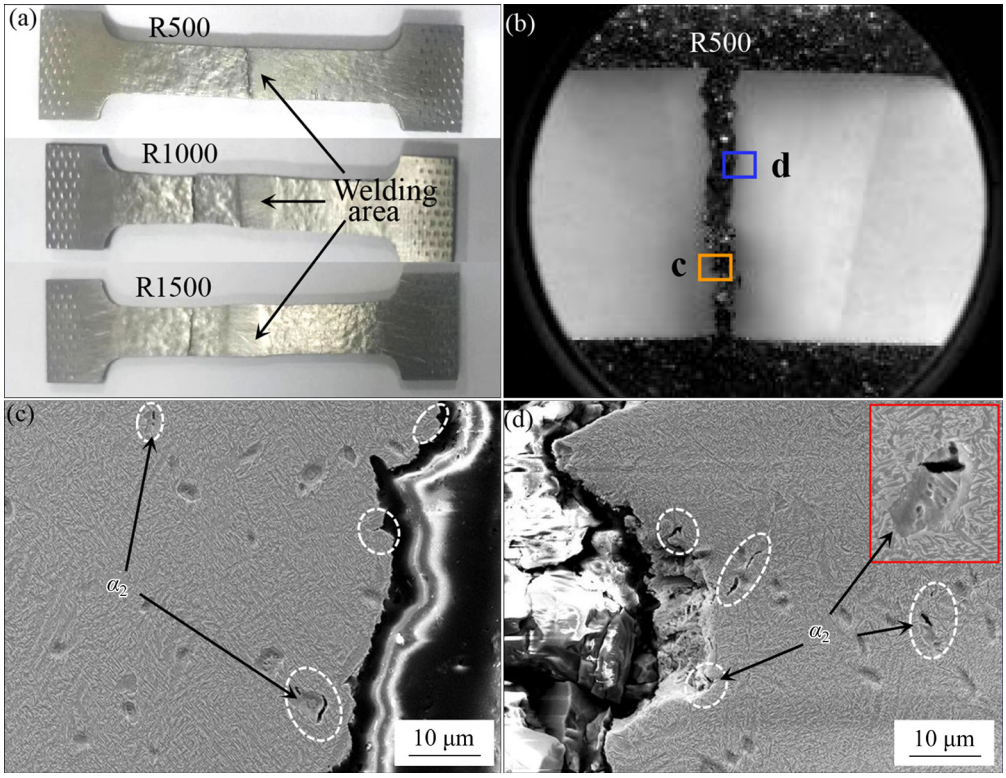


**Fig. 11** Photos of as-annealed joints after tensile test (a); Macrostructure of R500 (b); Magnification (c, d) of corresponding areas in (b)

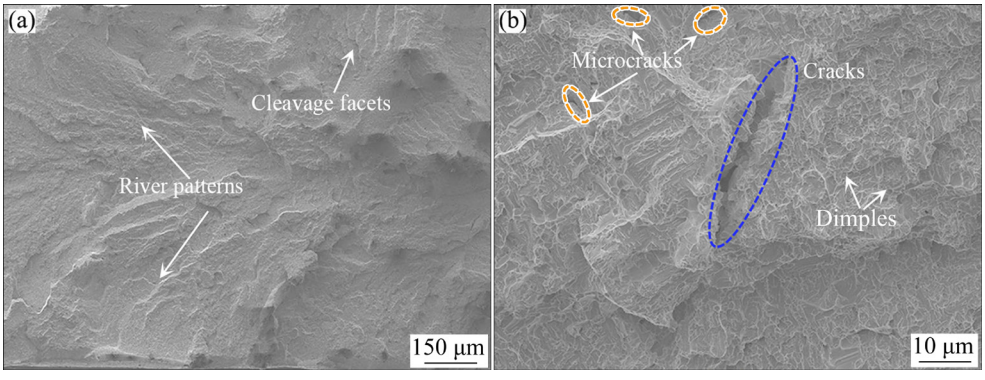


**Fig. 12** Fracture morphologies of as-annealed R500 at low (a) and large (b) magnifications

from the as-welded state (Figs. 8(a, d)), many river patterns and cleavage facets can be observed in the annealed joint. Besides, microcracks and fine dimples are also detected on the fracture surface (Fig. 12(b)). The annealing makes the fracture of R500 transform from a mixed mode of cleavage and intergranular fractures to the quasi-cleavage fracture.

*O* phase is the main strengthening phase in $Ti_2AlNb$ alloys [2,37]. A great quantity of fine *O* phases are precipitated in the welding area after the annealing treatment, making the strength of welding area much higher than that of the base metal area. Therefore, plastic deformation mainly occurs in the base metal of R1000 and R1500 during the tensile test. For R500, the $\alpha_2$ phase in HAZ is decomposed during the welding. Cracks are easy to generate at this place. The crack marked by a blue circle in Fig. 12(b) is generated in a decomposed $\alpha_2$ grain. As-welded R1500 fractures in TMAZ because of the anisotropic deformation microstructure. After annealing, *O* is re-precipitated, which strengthens the welding area effectively and correspondingly as-annealed R1500 shows excellent tensile performance. By comparing the microstructures and mechanical properties of various joints, it is clear that the decomposition of $\alpha_2$ phase and exceptionally severe deformation microstructure should be avoided during the welding and post-weld annealing treatment.

## 4 Conclusions

(1) Defect-free $Ti_2AlNb$ joints are obtained by continuous drive friction welding. The cross-sections of the as-welded joints consist of a weld zone (WZ), two thermo-mechanically affected zones (TMAZs) and two heat affected zones (HAZs). WZ is fully composed of recrystallization grains of *B*2 phase. TMAZ undergoes severe plastic deformation and is composed of deformed *B*2, $\alpha_2$ and some coarse *O* phase. In HAZ, only part of fine *O* phase is dissolved.

(2) When the joints welded at a rotational rate of 500, 1000 and 1500 r/min are subjected to tensile test, fracture takes place in HAZ, base metal and TMAZ, respectively. The joint welded at 1000 r/min has the best mechanical property, whose strength and elongation are both very close to those of the base metal.

(3) Post-weld annealing treatment makes fine O phase precipitate in the joint, and therefore significantly improved the tensile mechanical property, especially for the joints welded at 500 and 1500 r/min. The decomposition of $\alpha_2$ phase should be avoided during the welding, the decomposed $\alpha_2$ phase regions are prone to forming cracks during the tensile test and limit the improvement of mechanical performance of the joint.

### CRediT authorship contribution statement

**Zhi-qiang BU:** Methodology, Investigation, Data curation, Writing − Original draft; **Xiu-ping MA:** Investigation, Validation; **Jia-yun WU:** Investigation, Methodology; **Zhen LÜ:** Investigation; **Hu CHEN:** Investigation, Resources; **Jin-fu LI:** Conceptualization, Supervision, Writing − Review & editing, Funding acquisition.

### Declaration of competing interest

The authors declare that they have no known competing financial interests or personal relationships that could have appeared to influence the work reported in this paper.

### Acknowledgments

The authors are grateful for the financial supports from the Science and Technology Special Project, China (No. K19168), the National Science and Technology Major Project of China (No. 2017-VI-0004-0075), and the National Natural Science Foundation of China (No. 52231002).

### References

[1] BANERJEE D, GOGIA A K, NANDI T K, JOSHI V A. A new ordered orthorhombic phase in a $Ti_3Al$−Nb alloy [J]. Acta Metallurgica, 1988, 36(4): 871−882.

[2] WANG W, ZENG W D, XUE X, LIANG X B, ZHANG J W. Microstructure control and mechanical properties from isothermal forging and heat treatment of Ti−22Al−25Nb (at.%) orthorhombic alloy [J]. Intermetallics, 2015, 56: 79−86.

[3] GOYAL K, SARDANA N. Phase stability and micro-structural evolution of $Ti_2AlNb$ alloys — A review [J]. Materials Today: Proceedings, 2021, 41: 951−968.

[4] ZHANG Y L, FENG A H, QU S J, SHEN J, CHEN D L. Microstructure and low cycle fatigue of a $Ti_2AlNb$-based lightweight alloy [J]. Journal of Materials Science & Technology, 2020, 44: 140−147.

[5] DANG Z Y, QIN G L, MA H GENG P H. Multi-scale characterizations of microstructure and mechanical properties of Ti6242 alloy linear friction welded joint with

post-welded heat treatment [J]. Transactions of Nonferrous Metals Society of China, 2023, 33: 1114−1123.

[6] CAM G, CLEMENS H, GERLING R, KOCAK M. Diffusion bonding of γ-TiAl sheets [J]. Intermetallics, 1999, 7: 1025−1031.

[7] CAM G, IPEKOGLU G, BOHM K H, KOCAK M. Investigation into the microstructure and mechanical properties of diffusion bonded TiAl alloys [J]. Journal of Materials Science, 2006, 41(16): 5273−5282.

[8] WEI Z J, FANG W B, WANG H W, ZENG S Y. Microstructure and microhardness of $Ti_3Al$ matrix composites produced by XD$^{TM}$ synthesis [J]. Transactions of Nonferrous Metals Society of China, 2002, 12: 1138−1141.

[9] ZHANG H Y, YAN N, LIANG H Y, LIU Y C. Phase transformation and microstructure control of $Ti_2AlNb$-based alloys: A review [J]. Journal of Materials Science & Technology, 2021, 80: 203−216.

[10] ZHAO H Z, LU B, TONG M, YANG R. Tensile behavior of Ti−22Al−24Nb−0.5Mo in the range 25−650 °C [J]. Materials Science and Engineering A, 2017, 679: 455−464.

[11] LEI Z L, DONG Z J, CHEN Y B, ZHOU K, MA R. Effect of heat input on the microstructures and mechanical properties of laser welded $Ti_2AlNb$ alloys [J]. Rare Metal Materials and Engineering, 2014, 43(3): 579−584.

[12] EMURA S, ARAOKA A, HAGIWARA M. B2 grain size refinement and its effect on room temperature tensile properties of a Ti−22Al−27Nb orthorhombic intermetallic alloy [J]. Scripta Materialia, 2003, 48(5): 629−634.

[13] BOEHLERT C J. The phase evolution and microstructural stability of an orthorhombic Ti−23Al−27Nb alloy [J]. Journal of Phase Equilibria, 1999, 20: 101−108.

[14] HAGIWARA M, ARAOKA A, YANG S J, EMURA S, NAM S W. The effect of lamellar morphology on tensile and high-cycle fatigue behavior of orthorhombic Ti−22Al−27Nb alloy [J]. Metallurgical and Materials Transactions A, 2004, 35: 2161−2170.

[15] ZONG Y Y, WANG J W, SHAO B, TANG W, SHAN D B. Mechanism and morphology evolution of the O phase transformation in Ti−22Al−25Nb alloy [J]. Journal of Materials Science & Technology, 2021, 89: 97−106.

[16] BU Z Q, WU J Y, MA X P, LI Z, LI J F. Microstructure and mechanical properties of electron beam welded joints of $Ti_2AlNb$ alloy [J]. Journal of Materials Engineering and Performance, 2023, 32(12): 5329−5337.

[17] LI Y J, WU A P, LI Q, ZHAO Y, ZHU R C, WANG G Q. Effects of welding parameters on weld shape and residual stresses in electron beam welded $Ti_2AlNb$ alloy joints [J]. Transactions of Nonferrous Metals Society of China, 2019, 29: 67−76.

[18] LEI Z L, ZHANG K Z, ZHOU H, NI L C, CHEN Y B. A comparative study of microstructure and tensile properties of $Ti_2AlNb$ joints prepared by laser welding and laser-additive welding with the addition of filler powder [J]. Journal of Materials Science & Technology, 2018, 255: 477−487.

[19] CHEN W, CHEN Z Y, WU C C, LI J W, TANG Z Y, WANG Q J. The effect of annealing on microstructure and tensile properties of Ti−22Al−25Nb electron beam weld joint [J]. Intermetallics, 2016, 75: 8−14.

[20] LI Y J, WU A P, LI Q, ZHAO Y, ZHU R C, WANG G Q. Mechanism of reheat cracking in electron beam welded $Ti_2AlNb$ alloys [J]. Transactions of Nonferrous Metals Society of China, 2019, 29: 1873−1881.

[21] ÖZDEMIR N, SARSLMAZ F, HASCALK A. Effect of rotational speed on the interface properties of friction-welded AISI 304L to 4340 steel [J]. Materials & Design, 2007, 28: 301−307.

[22] SATHIYA P, ARAVINDAN S, NOORUL HAQ A N. Mechanical and metallurgical properties of friction welded AISI 304 austenitic stainless steel [J]. International Journal of Advanced Manufacturing Technology, 2005, 26: 505−511.

[23] ATES H, TURKER M, KURT A. Effect of friction pressure on the properties of friction welded MA956 iron-based superalloy [J]. Materials & Design, 2007, 28: 948−953.

[24] CHEN X, XIE F Q, MA T J, LI W Y, WU X Q. Effects of post-weld heat treatment on microstructure and mechanical properties of linear friction welded $Ti_2AlNb$ alloy [J]. Materials & Design, 2016, 94: 45−53.

[25] LI X, LI J L, JIN F, XIONG J T, ZHANG F S. Effect of rotation speed on friction behavior of rotary friction welding of AA6061-T6 aluminum alloy [J]. Welding in the World, 2018, 62: 923−930.

[26] LIU Y, ZHAO H Y, PENG Y, MA X F. Microstructure characterization and mechanical properties of the continuous-drive axial friction welded aluminum/stainless steel joint [J]. International Journal of Advanced Manufacturing Technology, 2019, 104: 4399−4408.

[27] LIANG Z D, QIN G L, GENG P H, YANG F, MENG X M. Continuous drive friction welding of 5A33 Al alloy to AZ31B Mg alloy [J]. Journal of Manufacturing Processes, 2017, 25: 153−162.

[28] LI W Y, WANG F F. Modeling of continuous drive friction welding of mild steel [J]. Materials Science and Engineering A, 2011, 528: 5921−5926.

[29] CHEN X, XIE F Q, MA T J, LI W Y, WU X Q. Microstructure evolution and mechanical properties of linear friction welded $Ti_2AlNb$ alloy [J]. Journal of Alloys and Compounds, 2015, 646: 490−496.

[30] BU Z Q, ZHANG Y G, YANG L, KANG J M, LI J F. Effect of cooling rate on phase transformation in $Ti_2AlNb$ alloy [J]. Journal of Alloys and Compounds, 2021, 893: 162364.

[31] LI W Y, MA T J, LI J L. Numerical simulation of linear friction welding of titanium alloy: effects of processing parameters [J]. Materials & Design, 2010, 31: 1497−1507.

[32] DU Z H, JIANG S S, ZHANG K F, LU Z, LI B Y, ZHANG D L. The structural design and superplastic forming/diffusion bonding of $Ti_2AlNb$ based alloy for four-layer structure [J]. Materials & Design, 2016, 104: 242−250.

[33] WANG W, ZENG W D, LI D, ZHU B, ZHENG Y P, LIANG X B. Microstructural evolution and tensile behavior of $Ti_2AlNb$ alloys based $\alpha_2$-phase decomposition [J]. Materials Science and Engineering A, 2016, 662: 120−128.

[34] DEY S R, ROY S, SUWAS S, FUNDENBERGER J J, RAY P K. Annealing response of the intermetallic alloy Ti−22Al−25Nb [J]. Intermetallics, 2010, 18: 1122−1131.

[35] ZHANG H Y, ZHANG Y R, LIANG Y H, LIU Y C. Influence of cooling rates on microstructure and tensile properties of a heat treated $Ti_2AlNb$-based alloy [J]. Materials Science and Engineering A, 2021, 817: 141345.

[36] SUI X C, LIU Q, LUO S Y, LIU Y K, LI Z L, KANG Q X, WANG G F. Achieving high ductility of $Ti_2AlNb$ sheet without sacrificing the tensile strength without post heat treatment [J]. Materials Science and Engineering A, 2022, 840: 142897.

[37] WANG W, ZENG W D, XUE C, LIANG X B, ZHANG J W. Designed bimodal size lamellar O microstructures in $Ti_2AlNb$ based alloy: Microstructural evolution, tensile and creep properties [J]. Materials Science and Engineering A, 2014, 618: 288−294.

# 不同转速下 $Ti_2AlNb$ 合金连续驱动摩擦焊焊接接头的显微组织和力学性能

卜志强[1]，马秀萍[2]，吴家云[2]，吕 榛[2]，陈 虎[1]，李金富[1]

1. 上海交通大学 材料科学与工程学院 金属基复合材料国家重点实验室，上海 200240；
2. 中国航发南方工业有限公司，株洲 412002

**摘 要**：采用连续驱动摩擦焊接方法焊接 $Ti_2AlNb$ 基合金，对不同焊接转速(500、1000 和 1500 r/min)下的焊接接头的显微组织和力学性能进行研究。结果表明：接头焊缝区(WZ)完全由再结晶的 *B*2 相组成，且 *B*2 晶粒尺寸随着转速的增加而减小；焊接过程中热力影响区(TMAZ)发生严重变形，大部分原始析出相溶解的同时，组织中出现明显的流线；热影响区(HAZ)中只有细小的 *O* 相发生溶解。转速为 1000 r/min 时，焊接接头力学性能最好，其强度和伸长率均接近母材；转速为 500 r/min 时，焊接接头的力学性能最差。焊后退火处理可以明显消除变形组织，并在接头中重新析出细小的 *O* 相，从而大幅提高接头的力学性能。拉伸过程中分解的 $\alpha_2$ 相容易成为裂纹萌生的源头，极大限制接头力学性能的提高。

**关键词**：$Ti_2AlNb$ 合金；连续驱动摩擦焊；显微组织；力学性能

**(Edited by Bing YANG)**